Journal of Molecular Liquids 270 (2018) 191–202

Contents lists available at ScienceDirect

Journal of Molecular Liquids

journal homepage: www.elsevier.com/locate/molliq

Molecular dynamics and density functional study of the structure of hairy particles at a hard wall

M. Borówko[a], W. Rżysko[a], S. Sokołowski[a,*], O. Pizio[b,1]

[a] Department for the Modelling of Physico-Chemical Processes, Maria Curie-Sklodowska University, Gliniana 33, Lublin, Poland
[b] Instituto de Investigaciones en Materiales, Universidad Nacional Autónoma de México, Circuito Exterior, 04510, Cd. de México, Mexico

ARTICLE INFO

Article history:
Received 21 August 2017
Received in revised form 21 November 2017
Accepted 23 November 2017
Available online 27 November 2017

Keywords:
Nanoparticles
Molecular dynamics
Density functional
Adsorption

ABSTRACT

We study models of hairy nanoparticles in contact with a hard wall. According to the first model the ligands are grafted to a spherical core, while in the second model they can slide over the core surface. Using Molecular Dynamics simulations we investigate the differences in the structure of both system close to the wall. In order to characterize the distribution of the ligands around the core we have calculated the end-to-end distances of the ligands and the lengths and orientation of the mass dipoles. Moreover, for the model with mobile ligands we also employed a density functional approach to obtain the density profiles. We have found that the proposed version of the theory is capable to predict the structure of the system with a reasonable accuracy.

1. Introduction

It is our honor to dedicate this manuscript to the memory of an extraordinary scientist and extraordinary person Prof. Lesser Blum. Two of us (S.S. and O.P.), in particular, would like to appreciate friendship, scientific and non-scientific discussions with Lesser during his trips to Europe and Mexico in past decades. Lesser Blum has made important contributions to the theory of liquids, solutions and theoretical electrochemistry. One of his interests was in the applications of the theory of chemical association aiming at modelling of architecture of species in complex liquids or describing peculiar intermolecular bonding, see e.g. [1–5]. Our present contribution heavily rests on using the ideas of association for the construction of hairy nanoparticles and focuses in the properties of such complex fluid close to a solid surface.

The behavior of nanoparticles at different interfaces has attracted strong interest in the last years, what is undoubtedly connected with scientific and technological importance of such systems [6,7]. Our better understanding the structure and thermodynamic properties of nanoparticles at interfaces can be crucial for getting deeper knowledge on complex physical processes like heterogeneous catalysis, biological surface activity, biosensing and self-assembly [8–12].

Despite the great effort devoted to numerous experimental investigation of the adsorption, assembly and dynamics of nanoparticles at interfaces [13–19], a clear understanding of the rules governing the behavior of nanoparticles at interfaces and development of theoretical tools to describe and to predict their adsorption at solid surfaces is still an open challenge.

Among different kinds of nanoparticle one can distinguish the so-called hairy nanoparticles, that is the nanoparticles built of spherical central units (cores) functionalized with organic ligands (chains). Hairy nanoparticles are good candidates for developing relatively simple coarse-grained models describing their architecture. Both cores and segments of chain ligands can be treated as spherical units, bonded by imposing simple (e.g., harmonic) potentials. Indeed, the structure of chains' brush grafted to the core has been studied in several works employing simple models by theoretical methods, as well as by computer simulations, cf. Refs. [20–23]. Usually, theoretical description has been based on Density Functional approaches.

* Corresponding author.
E-mail address: stefan.sokolowski@gmail.com (S. Sokołowski).
[1] On sabbatical leave from Instituto de Quimica de la UNAM

https://doi.org/10.1016/j.molliq.2017.11.146
0167-7322/

Density Functional Theory (DFT) is a statistical-mechanical conceptual framework to analyze structure and thermodynamic properties of fluids. DFT can be applied to a wide range of interfacial phenomena, as well as problems in adsorption, colloidal science and phase transitions in fluids. The theory was first used to study simple fluid interfaces in the late 1970s [24]. Since then, numerous versions of DFTs have been applied to cover a wide range of fields [25,26] and to study more and more complex problems. Among different systems investigated by means of DFT approaches we mention here about associating fluids [27–29], ionic fluids, [27,30] systems involving dipolar molecules, [31] Janus particles, [32,33] and systems with polyatomic molecules [34,35] Also, several novel efficient and accurate algorithms for solving density profile equation have been developed, see e.g. [36–38].

Recently, DFTs have been employed to describe systems with molecules of quite complex geometries [39–42], or even geometrical constructs. For example, Marechal et al. [43] proposed two versions of DFT to study rod-like triangular prisms and to gauge the effect of the cross section of the rods on liquid crystal phase behavior.

One of the first approaches to describe bulk systems involving star and branched polymeric molecules was proposed by Blas and Vega [44]. According to their model, the excess Helmholtz free energy due to intramolecular connectivity is separated into two contributions, one accounting for the formation of the articulation vertex, and a second one due to the formation of arms. The approach of Blas and Vega was extended to the case of nonuniform systems by Malijevský et al. [45] Later, several alternative DF approaches for polymers with complex geometries have been developed, cf. [46–49] Majority of the works cited above have assumed equal sizes of all segments of polymers. However, Jiang et al. [50] developed a DFT for rod-coil copolymers with different size segments. Their approach combines a modified fundamental measure theory for the excluded-volume effects [51,52], Wertheim's [53] first-order thermodynamics perturbation theory for the chain connectivity and the mean field approximation for van der Waals attraction. The architecture of star polymers and of hairy nanoparticles is similar. Both type of particles consist of a central particles (the articulation vertex or the core molecule) and a number of chains attached to it. Therefore, a theory that combines the approaches of Refs. [45,50] seems to be a promising candidate for describing nonuniform system involving hairy nanoparticles.

In this work we study two model of hairy nanoparticles confined at a hard wall. According to the first model the ligands are attached to a core at fixed grafting points, whereas in the second – they can "slide" over the core surface. In both cases we neglect the presence of a solvent. In other words, both models belong to the class of models with an implicit solvent. According to that treatment the presence of a continuous solvent is accounted for by introducing "effective" interactions between nanoparticles. Systems with mobile ligands, such as CdSe/CdS core–shell particles with a brushlike layer of polyethylene oxide or branched polyethyleneimine and others have been studied previously. [54–60] However, examples of the systems with ligands attached at fixed points are given in Refs. [61,62] We already know that ligands mobility can change the effective interactions between nanoparticles [63].

Our purpose is two-fold. First, using molecular dynamics simulations we compare the structure of the molecules in layers adjacent to the wall. In order to estimate how the distribution of segments around nanoparticles depends on the ligands mobility, we evaluated the so-called mass dipoles [64–66] and computed the histograms of their lengths and orientations with respect to the wall. Next, for the model with mobile ligands we have compared the results of simulations with theoretical predictions obtained from a version of DFT. The organization of our work is as follows. In Section 2.1 we describe the two models in details and the method of simulations. Section 2.2 is devoted to the description of the DFT used in our work. Next, Section 3.1 presents simulation data for both models in question and Section 3.2 compares the simulation data with theoretical predictions. The paper is summarized in Section 4.

2. Theoretical description

2.1. Model and simulations

A single particle is build of a spherical core of diameter σ_0 and L chains (ligands) grafted at its surface. Each single chain is built of N tangentially jointed spherical segments of equal diameters $\sigma_s \equiv \sigma$. All the ligands are identical. The first segment of each ligand is grafted to the core and the grafting distance is $d = (\sigma_0 + \sigma)/2$.

We study two models. In the first one, abbreviated as the model M in what follows, the tethered segments can "slide" over the surface of the sphere of diameter $2d$. In the second case (the model F) the first segments of ligands are rigidly bonded at the vertices of a regular, convex polygon inscribed into the sphere of the diameter $2d$. According to F model the angles $\alpha_{0,ij}$ between the consecutive vectors $\mathbf{b}_i$ and $\mathbf{b}_j$ pointing from the core center to the center of the grafted segments i and j are fixed. We consider the systems M and F with six ligands, $L = 6$, each composed of $N = 6$ segments. In the model F the ligands are attached at the vertices of an octahedron.

The core-grafted segment, $u_{0s}^{(b)}$, and the segment-segment, $u_{ss}^{(b)}$ bonds are assured by imposing the harmonic potentials

$$u_{0s}^{(b)} = k_{0s}(r-d)^2, \tag{1}$$

and

$$u_{ss}^{(b)} = k_{ss}(r-\sigma)^2. \tag{2}$$

In the case of the model F the angles between grafted segments i and j are kept by assuming the harmonic angular potentials

$$u_{ij}^{(a)}(\alpha_{ij}) = k_a(\alpha_{ij} - \alpha_{0,ij})^2, \tag{3}$$

where $\alpha_{0,ij}$ is the equilibrium angle between two nearest bonds $(\pi/2)$.

The non-bonded segment-segment (ss), segment-core ($0s$) and core-core (00) interactions were modelled by Lennard-Jones (12,6) potentials

$$u_{kl}(r) = \begin{cases} 4\varepsilon_{kl}\left[(\sigma_{kl}/r)^{12} - (\sigma_{kl}/r)^6\right], & r < r_{cut,kl}, \\ 0, & \text{otherwise}, \end{cases} \tag{4}$$

where $kl = ss, 0s, 00$ and r is the distance between interacting species and ε_{kl}'s are the energy parameters. We assume the Lorentz-Berthelott combining rules for the cross interactions, i.e., $\sigma_{0s} = (\sigma_{00} + \sigma_{ss})/2$ and $\varepsilon_{0s} = \sqrt{\varepsilon_{00}\varepsilon_{ss}}$. According to our notation $\sigma_{00} \equiv \sigma_0$, $\sigma_{ss} \equiv \sigma_s$, $\varepsilon_{00} = \varepsilon_0$ and $\varepsilon_{ss} = \varepsilon_s$. If the cut-off distances are $r_{cut,kl} = \sigma_{kl}$, then the interactions are purely repulsive.

The van der Waals potential energy involves intramolecular and intermolecular segment-segment and segment-core interactions. The intramolecular contribution is the sum of the potentials (4) and the summation is carried out over all entities (core and segments) within a given molecule. Determining intramolecular energies have also assumed that the entities that are directly bonded, do not interact via the Lennard-Jones forces.

The system with hairy particles was confined between two hard planar walls, located at $z = 0$ and $z = L_z$. Thus, the wall-core and the wall-segment potentials are given by

$$v_0(z) = \begin{cases} 0, & \sigma_0/2 < z < L_z - \sigma_0/2, \\ \infty, & \text{otherwise}, \end{cases} \tag{5}$$

and

$$v_s(z) = \begin{cases} 0, & \sigma/2 < z < L_z - \sigma/2, \\ \infty, & \text{otherwise} \end{cases}. \tag{6}$$

The parameters $\sigma = \sigma_s$ (the diameter of the segments) and $\varepsilon = \varepsilon_0$ (the core-core energy parameter) are the units of the length and of the energy, respectively. The mass of the core molecule, m was assumed to be the unit of mass. The mass of each segment was (arbitrary) set equal $m/10$. The dynamic properties of the system would depend on the accepted ratio of the masses, but our interest is only in the evaluation of the equilibrium structure of the system. In our study $\sigma_0 = 4\sigma$ and $\varepsilon_s = \varepsilon/10$. Moreover, we assumed purely repulsive core-segment and segment-segment interaction. In other words, the segments of the ligands "screen" attractive core-core forces. The cut-off distance of the latter forces was equal $3\sigma_{0s}$. The constants k_{0s} and k_{ss} were $1000\varepsilon/\sigma^2$, while the constant k_a was $1000\varepsilon/(\text{radian}^2)$.

The reduced length, time and temperature and energy are respectively defined as follows $r^* = r/\sigma$, $\tau^* = \tau\sqrt{\varepsilon/(m\sigma^2)}$ and $T^* = kT/\varepsilon$. All the calculations were performed at $T^* = 2$.

The Molecular Dynamics simulations were carried out in a cuboidal box of the size $L_x \times L_x \times L_z$ using LAMMPS [67,68] package. The temperature was controlled by Berendsen thermostat. The distance L_z was large enough to assure independence of the particles at both walls. It ranged from 120σ to 240σ. In the majority of the runs the box dimension L_x was 120σ, sometimes a bigger box was also used. The total number of particles varied from 10,000 to 15,000. (Since each nanoparticle is built of 1 core atom and 36 segments, the total number of simulated atoms was 37 times larger.) Usually, the simulations were carried with $\Delta\tau^* = 0.001$. Note that in simulations the wall-core and wall-segment interactions, Eqs. (5) and (6), were modelled using LAMMPS *wall/reflect* utility. After equilibration (usually, for 10^7 timesteps) the production runs for at least 10^8 timesteps were performed.

During production runs we evaluated the local densities of particular entities, a pseudo-two dimensional radial distribution functions in the slabs of 1σ wide in planes parallel to the walls. Moreover, we have computed the end-to-end distances, $d_e(z)$, averaged over all ligands within a given particle in function of the distance of the core from the "bottom" (at $z = 0$) wall. Next, for the model M we have calculated the histograms of the distances $R_d(z)$ between tethered segments for a set of z values. For the model F the distribution of the distances $R_d(z)$ exhibits two very sharp Gaussian peaks at $R_d = 2d$ and $R_d = d\sqrt{2}$; the width of these peaks is determined by the values of the force constants k_{0s} and k_a.

For each particle we also have calculated the mass dipole. According to its definition [64–66] we determine the center of mass of all the segments, $\mathbf{R}_l$, first, and then define the mass dipole vector as $\mathbf{R}_m = \mathbf{R}_l - \mathbf{r}_0$, where $\mathbf{r}_0$ is the position of the core. The vector $\mathbf{R}_m$ characterizes the symmetry of the distribution of the segments. The orientation of the mass dipole of the nanoparticles can be described the distribution function $P(z,t)$, where $t = cos(\theta)$ and θ is the angle between the vector $\mathbf{R}_m$ and the unit vector perpendicular to the bottom wall. In order to probe uncorrelated configurations, the accumulation of the structural quantities was carried out after 50 consecutive timesteps.

2.2. Density functional theory

The density functional theory employed here is closely related to the approach described previously [45]. In contrast to simulations, the length of the bonds in the theory is constant. As in simulation, the core molecule is labeled by the subscript 0 and the consecutive segments starting from the tethered segment – by the subscripts $1, 2, \ldots, N$. The ligands (arms), however, are distinguished by the superscripts $1, 2, \ldots, L$. In our model all the arms are identical. In the theory the intramolecular bonding potential, $V_b(\mathbf{R})$, has the form [45,50]

$$\exp\left[-V_b(\mathbf{R})/kT\right] = \prod_{i=1}^{L} \frac{\delta\left(\left|\mathbf{r}_0 - \mathbf{r}_1^{(i)}\right| - d\right)}{4\pi d^2} \prod_{j=1}^{N-1} \frac{\delta\left(\left|\mathbf{r}_j^{(i)} - \mathbf{r}_{j+1}^{(i)}\right| - \sigma\right)}{4\pi\sigma^2}, \tag{7}$$

where $\mathbf{R} = \left(\mathbf{r}_0, \left\{\mathbf{r}_j^{(i)}\right\}\right)$, $i = 1, 2, \ldots L$, $j = 1, 2, \ldots, N$ denotes the positions of the core and all ligands' segments. We stress that the potential (7) corresponds to the model M. The intramolecular binding potential for the model F, however, should additionally contain the angular-dependent terms, cf. Ref. [50].

The second difference between the models used in theory and simulation results from the treatment of segment-segment, segment-core and core-core van der Waals forces. The theory is based [45,50] on perturbational treatment, according to which the function (4) is divided into repulsive, reference part and the attractive contribution (perturbation),

$$u_{kl}^{(att)}(r) = \begin{cases} 0, & r < \sigma_{kl}, \\ u_{kl}(r), & \text{otherwise}, \end{cases}. \tag{8}$$

In our approach the reference potential is just the hard-sphere potential with the hard-sphere diameter equal σ_{kl}. We are aware that more sophisticated treatments exist [69], but since we are interested in determination of the structure of the particles at temperature much higher than the bulk critical temperature, we have decided to employ this simplest division.

In the systems studied here, the division of the potential into attractive and repulsive parts applies only to the core-core interactions, while the core-segment and segment-segment van der Waals interactions are modelled by the hard-sphere potentials.

The grand potential of the system, Ω, is as a functional of the local density $\rho(\mathbf{R})$,

$$\Omega\left[\rho(\mathbf{R})\right] = F_{id}\left[\rho(\mathbf{R})\right] + F_{ex}\left[\rho(\mathbf{R})\right] + \int \mathrm{d}\mathbf{R}\left[V_{ext}(\mathbf{R}) - \mu\right]\rho(\mathbf{R}). \tag{9}$$

In the above μ is the configurational chemical potential, $V_{ext}(\mathbf{R})$ is the external potential field, being the sum of the external potential energies acting on the core and all the segments,

$$V_{ext}(\mathbf{R}) = v_0(\mathbf{r}_0) + \sum_{i=1}^{L}\sum_{j=1}^{N} v_s\left(\mathbf{r}_j^{(i)}\right), \tag{10}$$

$F_{id}[\rho(\mathbf{R})]$ is the ideal free energy,

$$F_{id}\left[\rho(\mathbf{R})\right]/kT = \int \mathrm{d}\mathbf{R}\rho(\mathbf{R})\left[V_b(\mathbf{R}) + \ln(\rho(\mathbf{R})) - 1\right], \tag{11}$$

and $F_{ex}[\mathbf{R}]$ is the excess free energy. The latter functional is the sum of the contributions resulting from hard-sphere repulsion between all

the atomistic entities (cores and segments), $F_{hs}[\rho(\mathbf{R})]$, the contribution due to the intramolecular binding, $F_b[\rho(\mathbf{R})]$, and the contribution arising from attractive interactions between the species, $F_{att}[\rho(\mathbf{R})]$.

To proceed, we define the total, angular averaged local density, $\rho_t(\mathbf{r})$ by

$$\rho_t(\mathbf{r}) = \rho_0(\mathbf{r}) + \sum_{i=1}^{L}\sum_{j=1}^{N}\rho_j^{(i)}(\mathbf{r}) = = \int d\mathbf{R}\delta(\mathbf{r}-\mathbf{r}_0)\rho(\mathbf{R}) + \sum_{i=1}^{L}\sum_{j=1}^{N}\int d\mathbf{R}\delta\left(\mathbf{r}-\mathbf{r}_j^{(i)}\right)\rho(\mathbf{R}), \quad (12)$$

Since all ligands have the same length and all segments are identical, then for both models M and F studied here the local densities $\rho_j^{(i)}(\mathbf{r})$ do not depend on the ligand number, i. Therefore, we introduce the total densities of segments j, irrespective to which ligand they belong to, $\rho_j(\mathbf{r}) = \sum_{i=1}^{L}\rho_j^{(i)}\rho_j^{(i)}(\mathbf{r})$.

Following refs. [45,50] the excess free energy contribution $F_{hs}[\rho(\mathbf{R})]$ is evaluated by using Rosenfeld's approach that requires the introduction of four scalar and two vector weighted densities and the White-Bear theory for the free energy of hard-spheres [51,52]. Because this approach is quite standard, we refer a reader to the original publications [50–52]. We only recall that it uses four scalar $n_\alpha(\mathbf{r})$, $\alpha = 0,1,2,3$, and the two vector, $\mathbf{n}_{V\gamma,m}(\mathbf{r})$, $\gamma = 1,2$, weighted densities are given by

$$n_\alpha(\mathbf{r}) = n_{\alpha,0}(\mathbf{r}) + \sum_{j=1}^{N} n_{\alpha,0}(\mathbf{r}) = \int d\mathbf{r}'\rho_0(\mathbf{r}')w_{\alpha,0}\left(|\mathbf{r}-\mathbf{r}'|\right) + \sum_{j=1}^{N}\int d\mathbf{r}'\rho_j(\mathbf{r}')w_{\alpha,j}\left(|\mathbf{r}-\mathbf{r}'|\right) \quad (13)$$

and

$$\mathbf{n}_{V\gamma}(\mathbf{r}) = \mathbf{n}_{V\gamma,0}(\mathbf{r}) + \sum_{j=1}^{N}\mathbf{n}_{V\gamma,j}(\mathbf{r}) = \int d\mathbf{r}'\rho_0(\mathbf{r}')\mathbf{w}_{V\gamma,0}\left(|\mathbf{r}-\mathbf{r}'|\right) + \sum_{j=1}^{N}\int d\mathbf{r}'\rho_j(\mathbf{r}')\mathbf{w}_{V\gamma,j}\left(|\mathbf{r}-\mathbf{r}'|\right), \quad (14)$$

where the scalar, $w_{\alpha,m}(|\mathbf{r}-\mathbf{r}'|)$, and vector, $\mathbf{w}_{V\gamma,j}(|\mathbf{r}-\mathbf{r}'|)$ weight functions are given in Refs. [50,52].

The free energy resulting from attractive intermolecular forces can be described by using a mean-field approximation. In our case

$$F_{att}[\rho(\mathbf{R})] = \frac{1}{2}\left\{\int d\mathbf{r}_0\rho_0(\mathbf{r}_0)\int d\mathbf{r}_0'\rho_0(\mathbf{r}_0')\,u_{00}^{(att)}\left(|\mathbf{r}_0-\mathbf{r}_0'|\right)\right\}. \quad (15)$$

The free energy contribution due to the intramolecular connectivity is approximated by the expression resulting from Wertheim's theory of association, generalized [45,50,53] to nonuniform fluids

$$F_b/kT = \int d\mathbf{r}\left[\frac{L-LN}{LN+1}n_0(\mathbf{r})\xi(\mathbf{r})\ln y_{hs}(\sigma,\sigma,\{n_\alpha\}) - \frac{L}{LN+1}n_0(\mathbf{r})\xi(\mathbf{r})\ln y_{hs}(\sigma,\sigma_0,\{n_\alpha\})\right], \quad (16)$$

where $\xi(\mathbf{r}) = 1 - \mathbf{n}_{V2}(\mathbf{r})\cdot\mathbf{n}_{V2}(\mathbf{r})/n_2^2(\mathbf{r})$ and $lny_{hs}(\sigma,\sigma,\{n_\alpha\})$ and $lny_{hs}(\sigma,\sigma_0,\{n_\alpha\})$ are the contact values of the hard-sphere cavity functions, i.e., the values of $y(s,s_1,\{n_\alpha\})$ at the distance $(s+s_1)/2$ and they are given by Eq. (11) of Ref. [50].

The density profile equations are obtained minimizing the grand canonical potential, $\delta\Omega/\rho(\mathbf{R}) = 0$. For the system with local densities varying in one dimension, z, we obtain

$$\rho_0(z) = \exp(\mu/kT)h_0(z)\left[G^{(N+1)}(z)\right]^L \quad (17)$$

and

$$\rho_j^{(i)}(z) = \exp(\mu/kT)h_j^{(i)}(z)G^{(N+1-j)}(z)\tilde{G}^{(j+1)}(z), \quad (18)$$

where

$$h_j^{(i)}(z) = \exp\left\{-\left[\delta F_{ex}/\delta\rho_j^{(i)}(z) + v_s(z)\right]/kT\right\},$$
$$h_0 = \exp\left\{-\left[\delta F_{ex}/\delta\rho_0(z) + v_0(z)\right]/kT\right\}$$

and where $h_0(z) \equiv h_0^{(i)}(z)$. We recall, that according to our model the functions $h_j^{(i)}$ are independent of the ligand index i; thus we can drop the superscript (i) in the symbols of these functions, $h_j \equiv h_j^{(i)}$. The functions $G^{(j)}$ and $\tilde{G}^{(j)}$ are given by the following recurrence relations

$$G^{(j)}(z) = \int dz' h_{N-j+2}(z')\frac{H\left(d_{N-j}-|z-z'|\right)}{2d_{N-j}}G^{(j-1)}(z'), \quad (19)$$

for $j = 2,3,\ldots,N$ and $G^{(1)}(z) \equiv 1$,

$$\tilde{G}^{(2)}(z) = \int dz h_0(z')\frac{H\left(d_0-|z-z'|\right)}{2d_0}\left[G^{(N+1)}(z')\right]^{L-1}, \quad (20)$$

and, for $j > 2$,

$$\tilde{G}^{(j)}(z) = \int dz h_j(z')\frac{H\left(d_j-|z-z'|\right)}{2d_j}\tilde{G}^{(j-1)}(z'). \quad (21)$$

In the above $H(d-z)$ is the step-function and $d_0 = d$ and $d_j = \sigma$ for $j = 2,3,\ldots,N$. Details on the numerical methods are given in Refs. [45,50].

In contrast to the approach of Ref. [45], where the second-order Wertheim theory was employed to determine the free energy contribution due to intramolecular bonding, the theory outlined above is based on the first-order approach. The second-order term in Ref. [45] was introduced to take into account the geometry of the points of tethering. An alternative treatment was proposed by Jiang et al. [50], where the geometry of the particles was assured by imposing angular bonds and angular-dependent bonding potential, cf. Eq. (7) of Ref. [50]. Neglecting the angular-dependent binding potential corresponds to the model M with "mobile" ligands. It is also possible to generalize the theory to the model F, following the ideas of Jiang et al. However, in the case of the ligands tethered at the vertices of an octahedron such a generalization would require introduction of binding potentials and each of them should be a function of two angles. Consequently, the density profile equations would appear to be much more complicated and cumbersome for an efficient numerical work. For this reason we have limited the application of the theory to the model M. In numerical calculations we have used the Fast Fourier Transform method to calculate all convolution integrals and the grid size equal to 0.02σ.

3. Results and discussion

3.1. Computer simulations: a comparison of two models

In this part of our work we discuss how the structure of particles at the wall depends on mobility of ligands. In Figs. 1 and 2 we display

the simulated density profiles of cores (parts a), of all segments (parts b),

$$\rho_s(z) = \sum_{j=1}^{N} \rho_j(z), \tag{22}$$

and the tethered segments (parts c) for the systems involving particles with fixed (Fig. 1) and mobile (Fig. 2) ligands. The color codes of consecutive lines are explained in parts a. The bulk densities, $\rho_{0b}\sigma_0^3$, have been evaluated by averaging the profiles in the region of z-values from $L_z/2 - 10\sigma$ to $L_z/2 + 10\sigma$.

The inset to Fig. 1a shows how the position of the first maximum of $\rho_0(z)$ changes with the bulk density, while the inset to Fig. 2a displays the excess adsorption isotherms of the cores

$$\Gamma_0 = \int_0^{L_z/2} dz\,[\rho_0(z) - \rho_{0b}] \tag{23}$$

for two models is question.

Except for very low densities ρ_{0b} the differences between density profiles for two models in question are significant (the structure of both systems at very low densities is discussed below, cf. Fig. 7).

Due to ligands mobility in the model M, the distance of the closest approach of cores to the wall is the same as for the cores without ligands, $d_c^{(M)} = \sigma_0/2 = 2\sigma$. When a particle is approaching the wall, the ligands can move to the other part of the core and the core can "touch" the wall. Of course, re-arrangement of the ligands is impossible for F particles. In this case the distance of the closest approach is $d_c^{(F)} = d\sqrt{2}/2 + \sigma/2 \approx 2.27\sigma$. At higher bulk densities ρ_{0b} the first maximum of $\rho_0(z)$ of M particles (Fig. 2a) is at the distance of the closest approach, $d_c^{(M)}$ and with this respect the particles behave like spheres at a hard wall. At low bulk densities the first maximum of $\rho_0(z)$ shifts toward higher distances from the wall, but except for very low ρ_{0b} we observe a pronounced jump of $\rho_0(z)$ at $z = d_c^{(F)}$.

For F particles (Fig. 1a), however, the first maximum appears at the distance z_{max1} that is definitely higher than $d_c^{(F)}$ and for lower wall-core distances, $z < z_{max1}$, local densities decay smoothly to zero. With an increase of ρ_{0b}, the value of z_{max1} decreases, but even at the highest investigated bulk density the value of z_{max1} is still well higher than $c_c^{(F)}$ (cf. the inset to Fig. 1a). The shape of the $\rho_0(z)$ profiles in Fig. 1 resembles the shape of the profiles of spherical particles in contact with soft, repulsive (or weakly attractive) wall.

The inset to Fig. 2a compares the excess adsorption isotherms of the cores. The adsorption is negative in the range of the investigated densities ρ_{0b}. Higher values of Γ_0 for the model M results from much higher first maximum of the density profiles $\rho_0(z)$ for this model.

The differences between the profiles for all segments, $\rho_s(z)$, (Figs. 1b and 2b) are less pronounced than the differences between the profiles of the cores. It is not surprising, since in both models the ligands are fully flexible and their segments move in the space in a similar manner (in both models identical restrictions resulting from bonds between consecutive segments exist). However, the density profiles of the tethered segments for the models F and M differ significantly (cf. Figs. 1c and 2c). For the model F and for high bulk densities the functions $\rho_1(z)$ exhibit well pronounced maxima at $z \approx 0.5\sigma$ and at $x \approx 4\sigma$. They correspond to the core particles located at (almost) the distance of the closest approach. Then, a part of tethered segments (marked as "1" in the schematic plot in the right upper corner of Fig. 1c.) is located directly at the wall, while some other part of segments (marked as "2") is at $z \approx 4\sigma$. However, for high bulk densities the profiles $\rho_1(z)$ for the model M exhibit a maximum at $z \approx 4.3\sigma$.

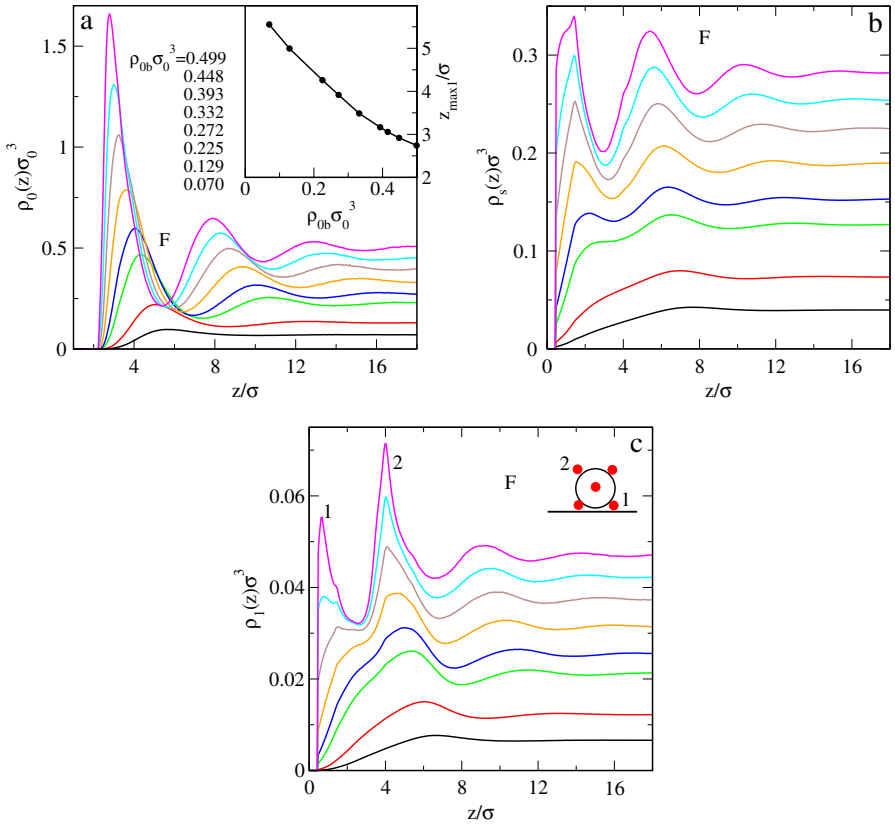

Fig. 1. Density profiles of cores (part a), of all segments of ligands (part b) and of tethered segments (part c). The calculations were carried out for the model F and for the bulk densities, ρ_{0b}, of cores given in part a, together with the description of the curves. The meaning of the curves in parts b and c is the same as in part a. The inset to part a shows how the position of the first maximum of $\rho_0(z)$, R_1, changes with the bulk density ρ_{0b}.

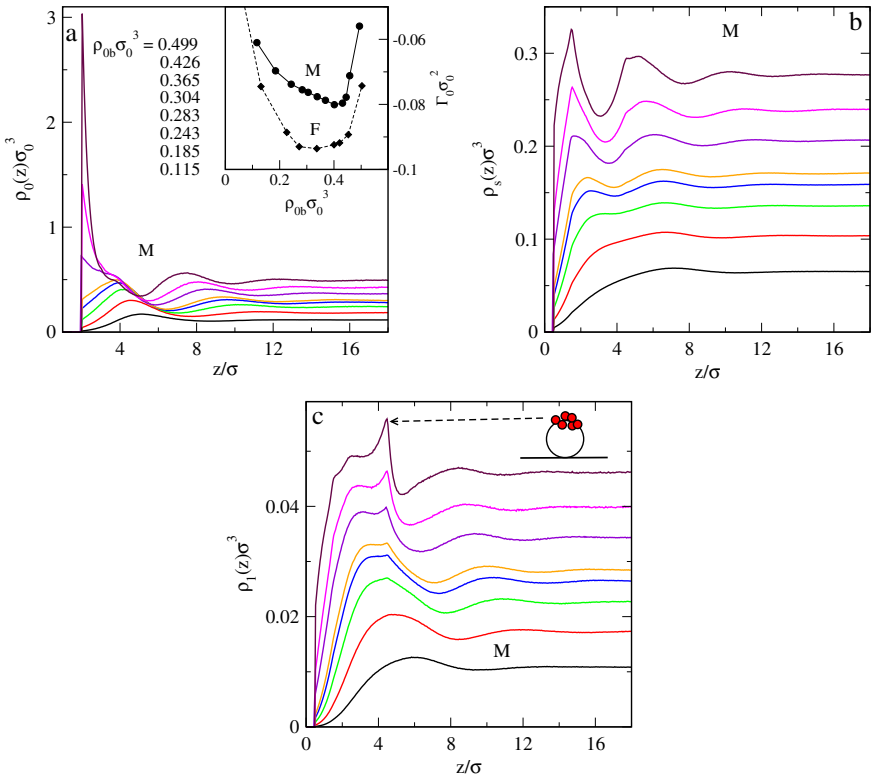

Fig. 2. Density profiles of cores (part a), of all segments of ligands (part b) and of tethered segments (part c). The calculations were carried out for the model M and for the bulk densities, ρ_{0b}, of cores given in part a, together with the description of the curves. The meaning of the curves in parts b and c is the same as in part a. The inset to part a shows the adsorption isotherms (Eq. (23)) for both models.

The location of this maximum is nearly equal to the average distance from the wall of the tethered segments for the core particle located at the distance of the closest approach, $d_c^{M)}$ and the tethered segments grouped at the hemisphere of the core opposite to the wall, cf. the schematic plot at the right upper corner of Fig. 2c.

Fig. 3 displays examples of the radial distribution function of the cores for the models F (part a) and M (part b) and at bulk densities $\rho_{0b}\sigma_0^3$, given in the figures. At each density the radial distribution functions were calculated for pairs of cores located in a layer of 0.8σ thick, parallel to the wall and centered at $z = z_{max1}$, the first maximum of the profile $\rho_0(z)$. At low densities the correlation functions for both models are similar. This is not surprising. Our recent studies [63] have indicated that the potentials of the mean force between a pair of nanoparticles are only slightly dependent on mobility of ligands. At higher densities the differences become more and more visible (note that the correlation functions are determined in the most dense part of the system). For the model F the core-core correlations are more pronounced than for the system M. Mobility of the ligands reduces the height of the first $g(r)$ peak and diminishes its oscillations.

It is interesting to see how the structure of segments around a single core changes with the distance of the core particle from the wall. As we have mentioned above, we have introduced the following measures to characterize the distribution of the segments, namely: (i) the histograms of the distances between the tethered segments, $R_d(z)$; (i) the end-to-end distances for ligands, $d_e(z)$, and, (iii) the mass dipoles, their length and orientation with respect to the vector perpendicular to the wall. Fig. 4a displays normalized histograms of

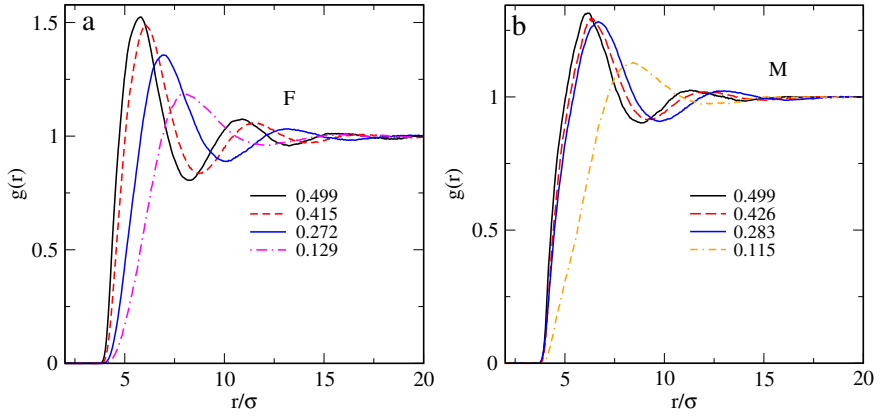

Fig. 3. Radial distribution functions between cores for models F (part a) and M (part b). The bulk densities, $\rho_{0b}\sigma_0^3$, of cores are given in the figures.

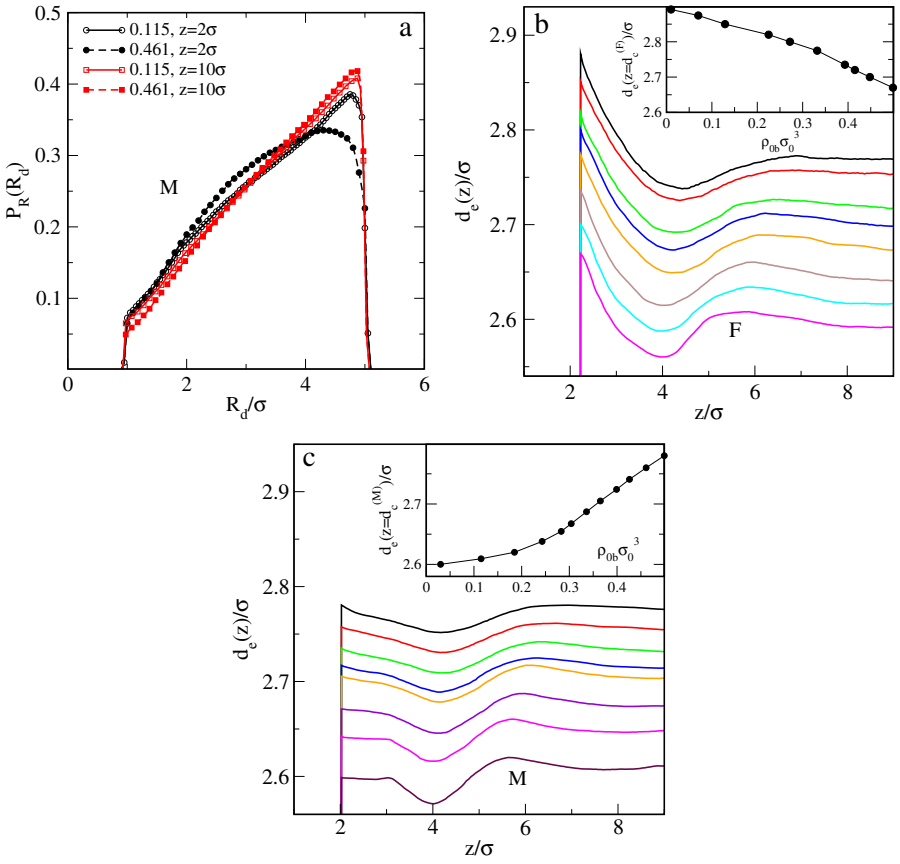

Fig. 4. Part a. Distributions of the distances between tethered segments, $P(R_d)$ for the systems M at two bulk densities $\rho_{0b}\sigma_0^3$ (the first numbers of the legend), at two distances from the surface, z (the second column of the legend). Parts b and c. The dependence of the average end-to-end distance, d_e, of the ligands on the distance of the core particle from the surface for the models F (part b) and M (part c). The insets show the dependence of d_e at the distance of the closest approach on bulk density. The meaning of the curves in parts b and c is the same as in Figs. 1a and 2a, respectively.

the distances between all pairs of tethered segments. The calculations were carried out at two bulk densities $\rho_{0b}\sigma_0^3$, given in the figure and at two distances of the core particles from the wall. The plots presented here are characteristic for other bulk densities. At larger distances from the wall the curves $P_R(R_d)$ are almost identical as those evaluated at $z = 10\sigma$. Moreover, also bulk density has a small influence on their shape. However, at small distances z (cf. the curves at $z = 2\sigma$) the shape of $P_R(R_d)$ is different from that in the bulk part of the system and changes with ρ_{0b}. In particular, number of pairs of tethered segments separated by the distance 5σ decreases significantly, especially for higher bulk density. This observation agrees with the suggested behavior of the molecules while discussing the profiles $\rho_1(z)$ (cf. Figs. 1c and 2c). We note that for the model F with ligands rigidly attached at the vertices of the octahedron the distribution $P_R(R_d)$ has the form $P_R(R_d) = \frac{12}{15}\delta(R_d - d\sqrt{2}) + \frac{3}{15}\delta(R_d - 2d)$ and is independent of z.

Fig. 4b and c show how the end-to-end distance changes with the distance of the core from the wall and with bulk density. The meaning of the lines is the same as in Figs. 1a (for the model F) and 2a (for the model M). An increase of ρ_{0b} causes a decrease of the values of $d_e(z)$ for both models. In fact, for a given model the plots $d_e(z)$ at different densities run almost in parallel. Smaller end-to-end distances mean that the ligands are "more coiled", thus for both models an increase of ρ_{0b} causes coiling of ligands.

Although the changes of end-to-end distances with z are rather small, they are more pronounced for the model F. In the case of the model M the minimization of the free energy of the system at a given ρ_{0b} is connected with the re-arrangement of the distribution of all entities in the space. The re-distribution of the segments occurs via "sliding" tethered segments and the changes of the configurations of remaining segments within a given ligand. The effect of "sliding" seems to be dominant, and, consequently the changes of d_e with z are small for this model. In the case of the model F, however, the "sliding" is impossible, and the effect of re-arrangement of non-tethered segments within particular ligands dominates.

In the case of the model F the end-to-end distances are the largest for the molecules located at the wall, i.e., the F ligands are more stretched at the wall and more coiled in the system interior. For the model M the situation is otherwise: the ligands are slightly more stretched in the bulk part of the system. However, except for the region close to the wall the values of $d_e(z)$ are slightly higher for M than for F molecules.

In Figs. 5 and 6 we have plotted the characteristics of the mass dipoles. By definition, the mass dipole characterizes the symmetry of the distribution of the segments around a core. The information that the length and the orientation of the mass dipoles provides is similar to the information resulting from the values of the diagonal elements of the matrix of the radii of gyration. In Fig. 5a, b (the model F) and 6a we show the histograms of the length of the mass dipoles as functions of the distance of the core from surface and of the bulk density. The length of the mass dipoles for the model M is almost two times larger than for the model F: at large bulk densities the maxima of $P_m(R_m)$ distributions lie around $R_m \approx 0.5\sigma$ for the model F and around $R_m \approx \sigma$ for the model M. For both models the lengths R_m are larger if the cores are at the distance of the closest approach. This is not surprising, since the presence of the wall enforces asymmetry

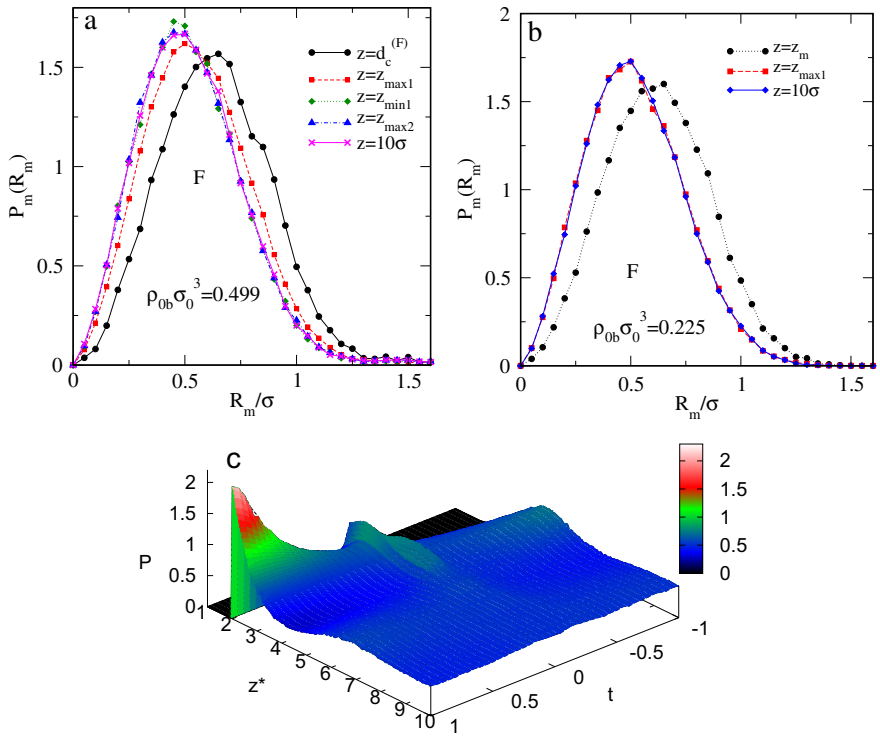

Fig. 5. Parts a and b. The histograms of the mass dipole lengths, R_m, for two bulk densities, $\rho_{0b}\sigma_0^3 = 0.499$ (part a) and $\rho_{0b}\sigma_0^3 = 0.225$ (part b). The results are for different distances of the core from the wall. Here z_{maxi}, $i = 1, 2$ is the position of the first and of the second maximum, while z_{min1} is the position of the first minimum of the profile $\rho_0(z)$. Part c. The distribution of the orientations of the mass dipoles, $P \equiv P(z, t)$, $z^* = z/\sigma$, $t = cos\theta$ for the system of the bulk density $\rho_{0b}\sigma_0^3 = 0.499$. All the calculations are for the model F.

in the distribution of ligands. At larger distances z the histograms $P_m(R_m)$ are almost indistinguishable. Moreover, they are only slightly dependent on the bulk density: the positions of the maximum of $P_m(R_m)$ are marginally smaller at higher bulk densities. In the case of more dense systems, the segments are "more compressed", and, consequently, the mass dipoles are slightly shorter.

Examples of the functions characterizing orientation of the mass dipoles is displayed in Fig. 5c and 6b. According to the definition of the angle θ ($t = cos\theta$), for $\theta = 0$ the majority of the segments is concentrated at the hemisphere of the core opposite to the wall, for $\theta = \pi/2$, the mass dipole is parallel to the wall, and for $\theta = \pi$ the mass dipole vector points toward the wall. In general, the orientation effects are more pronounced at higher bulk densities. At low densities they are very weak. We stress that these effect are much more pronounced for the model M (Fig. 6b),but general orientational tendency is similar for both models. In both models for the first layer core particles (i.e. for the particles adjacent to the wall) the predominant orientation of the mass dipoles is characterized by the angle $\theta = 0$ ($t = 1$). For the next layer the mass dipoles run in parallel to the wall, and for the third layer $\theta = \pi$. However, in the case of M molecules the distinguished orientation with $\theta = 0$ extends over larger than for the F molecules z distances than for the F molecules and a vicinity of the wall this orientation prevails. Unfortunately, physical interpretation of the differences is difficult.

As we have stressed above, at very low bulk densities the profiles for the systems F and M are quite similar (except for the profiles $\rho_0(z)$ at distances approaching the distances of the closest approach). In Fig. 7 we compare the profiles $\rho_0(z)$ (part a) and $\rho_s(z)$ (part b) for two models in question at $\rho_{0b}\sigma_0^3 = 0.0062$. Moreover, we have evaluated the "Boltzmann averaged" wall-core potentials of the mean force,

$$V_e(z)/kT = -\lim_{\rho_{0b}\to 0} \ln\langle\rho_0(z)/\rho_{0b}\rangle. \tag{24}$$

The linear extrapolation to zero bulk density was carried out performing simulations at two, extremely low bulk densities, $\rho_{0b}\sigma_0^3 = 0.001$ and 0.0005, and performing averaging over a huge number of timesteps.

The plot of $V_e(z)/kT$ for both models shows the inset to Fig. 7. For the model M the wall-core potential is effectively less repulsive when $z \to d_c^{(M)}$. This is the effect of segments' mobility - the segments can move to the hemisphere of the core opposite to the wall when the core approaches the closest approach distance.

At low ρ_{0b} the potential $v_e(z)$ can be used in the Boltzmann equation to evaluate the profiles

$$\rho_0(z) = \rho_{0b}\exp[-v_e(z)/kT]. \tag{25}$$

The Boltzmann profiles (25) are also shown in Fig. 7a. One could say that the agreement with simulations is quite satisfactory. However, there is one important discrepancy: even at so low bulk density the simulated profiles exhibit small maxima at $z = z_{max1} \approx 6.3\sigma$ while these maxima are absent in the case of the Boltzmann profiles. Thus, even at so low bulk density the linear (in bulk density) approximation is not accurate enough and higher-order terms of the virial local density expansion [70] should be taken into account.

In Fig. 7b we compare the profiles of the segments, $\rho_s(z)$ for the models F and M. The evaluated curves are very similar. However, the characteristics of the distribution of segments around cores are different in both models. The insets show (i) the histograms of the length of the mass dipoles at $z = z_{max1}$ and (ii) the dependences of the end-to-end distances of ligands as functions of the distance of the core particles from the wall. The course of the above characteristics is quite similar as in the case of higher densities, discussed above. However, it is surprising that the observed differences in the functions $P_m(R_m)$ and $d_e(z)$ for both models have so small influence on the

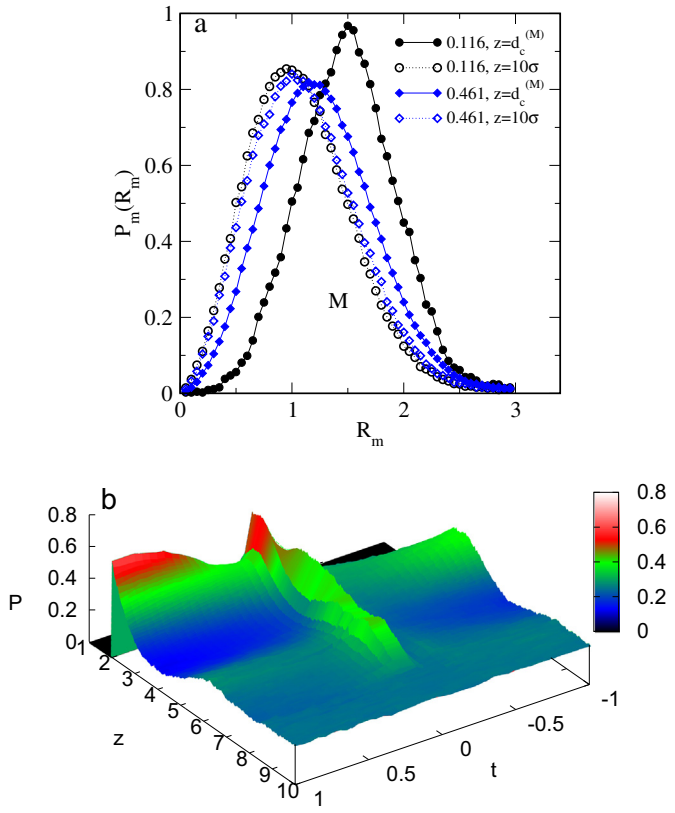

Fig. 6. Part a. The histograms of the mass dipole length, R_m, for two bulk densities, $\rho_{0b}\sigma_0^3 = 0.461$ and 0.116. The results are for two different distances of the core from the wall. Part b. The distribution of the orientations of the mass dipoles, $P \equiv P(z,t)$, $z^* = z/\sigma$, $t = cos\theta$ for the system of the bulk density $\rho_{0b}\sigma_0^3 = 0.461$. All the calculations are for the model M.

density profiles $\rho_s(z)$. Note that for the systems M and F at very low densities no pronounced orientation of the mass dipoles was found and the functions $P(z,t)$ (cf. Figs. 5c and 6b for higher densities) are almost constant and independent of z and t. For the sake of brevity the plots of these functions have been omitted.

3.2. Density functional theory results for the model M

Finally, we would like to compare the results of the Density Functional Theory with simulations. As we have mentioned above, the version of the theory is suited for the model M. Its extension would require introduction of angular-dependent binding potentials. In the case of a complex geometry like that for the model F this modification of the theory would lead to quite complex equations, prohibiting an effective numerical calculations. Moreover, the density functional theory has been developed for the Grand Canonical ensemble, where the chemical potential is an input variable that characterizes the bulk state of the system. In computer simulations we have determined the bulk densities and used them as input data in the density functional calculations. This leads to some inconsistencies of the theory and, consequently to errors, especially for the profiles at the wall, see [71].

In Fig. 8 we compare the local densities (reduced by the corresponding bulk values) of cores (part a), of all segments of ligands (part b) and of tethered segments (part c), evaluated from simulations (symbols) and from Density Functional Theory (lines). Note that the color codes of the curves is the case as in Fig. 2. Having in mind the differences between the models employed in simulations and theory (harmonic vs. fixed bonds) we can state that the agreement of theory with simulations is quite satisfactory. The observed discrepancies are smaller at higher densities, especially for profiles of segments. With an increase of the density the hard-sphere contribution to the system free energy becomes more and more significant and we know that the density functional theory of hard-sphere mixtures predicts quite well the structure near a hard wall.

At higher bulk densities the density profiles of segments $\rho_s(z)$ exhibit two cusps at $z/\sigma = 1.5$ and at $z/\sigma = 4.5$. In the case of the profiles of tethered segments the cusps appear $z/\sigma = 4.5$. These cups are clearly visible on the profiles evaluated from the theory, while simulated profiles are rounded off. The appearance of the cusps results from the existence of bonds. The cups at $z/\sigma = 1.5$ results from configurations where one segment is at the distance of the closest approach from the wall and its neighboring segment is located perpendicularly to the wall at the bonding distance from the first one. The cusps at $z/\sigma = 4.5$ correspond to a situation in which th e core remains at the distance of the closest approach from the wall and the tethered segment is located at the line perpendicular to the wall. In the case of the $\rho_s(z)$ profiles these cusps are less developed than the cusps at $z/\sigma = 1.5$ since the amount of tethered segments of $\frac{1}{6}$ of the total amount of segments; they are clearly seen on the $\rho_1(z)$ profiles. This rounding off the simulated profiles is the effects of "softness" of the bonds in the model employed in simulations. The cusps observed here have the same origin as the cusps in the profiles of tethered layer at a wall [72].

4. Summary

In this work we have performed molecular dynamics simulations of the structure of systems involving two kinds of hairy particles in contact with a hard wall. According to the first model (the model F), the tethering points of ligands were located at vertices of a regular octahedron, while in the case of the model M the ligands could "slide" along the sphere, representing the core of the nanoparticle. All calculations were carried out for an "implicit solvent models", i.e., no explicit solvent molecules were present in the system, but the interactions in the systems should be treated as effective, solvent mediated ones. Despite of the above simplifications the simulated systems comprised hundreds of thousands of "atomic species" (i.e. segments of ligands and cores). The interactions between particular segments, as well as between segments and cores were purely repulsive and the core-core interactions were modelled by Lennard-Jones (12,6) potential. In other words, the interactions with segments effectively "screen" direct core-core attractions.

For both systems in question we evaluated the density profiles of cores and of segments. To characterize the distribution of ligands around the core and to investigate how this distribution changes with the core distance from the wall we have determined the end-to-end distances of ligands and the lengths and orientations of the mass dipoles. Moreover, for the model M we have also computed the histograms of the distances between tethered segments.

At low bulk densities the density profiles of cores and of segments for both models are similar, although the distributions of segments around cores are different. In the limit of the bulk density $\rho_{0b} \to 0$ we have also evaluated the mean force core-wall potentials and checked if the Boltzmann approximation can be employed to describe the $\rho_0(z)$ profiles at low densities.

With increasing bulk densities the differences between the density profiles for the models F and M become more and more significant. With increasing bulk density the layers of F nanoparticles are compressed gradually toward the wall, similarly as the soft spheres would do. In other words the ligands attached at fixed positions act as an effective elastic shell, due to entropic elasticity of these polymer fragments. Consequently, one observes an increase of the effective diameter of F nanoparticle and effective softness of the surface. However, for the model M at higher bulk densities the location of the first local density peak is independent on the bulk density and

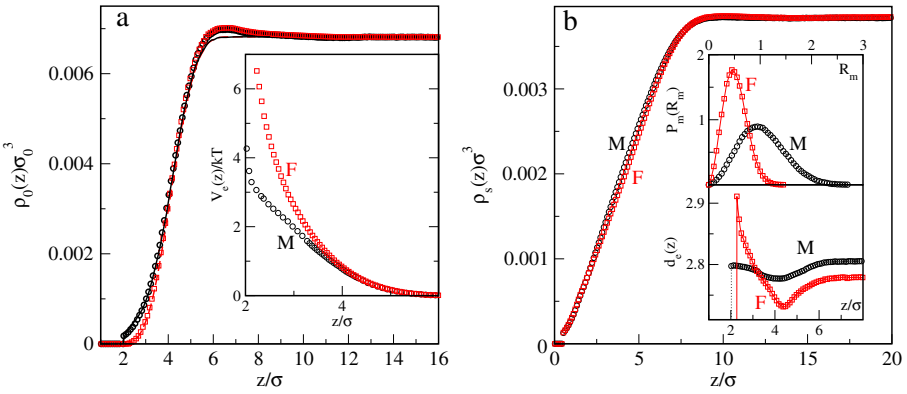

Fig. 7. Part a. Density profiles of cores (part a) and of all segments (part b) for the models M and F at a very low bulk density, $\rho_{0b}\sigma_0^3 = 0.00682$. In part a symbols denote simulation results and lines - the Boltzmann (Eq. 25) local densities. The inset to part a compares the potentials $V_e(z)$, while the insets to part b – the distribution of the lengths of mass dipoles at $z = z_{max1}$ and the end-to-end distances $d_e(z)$ for both models.

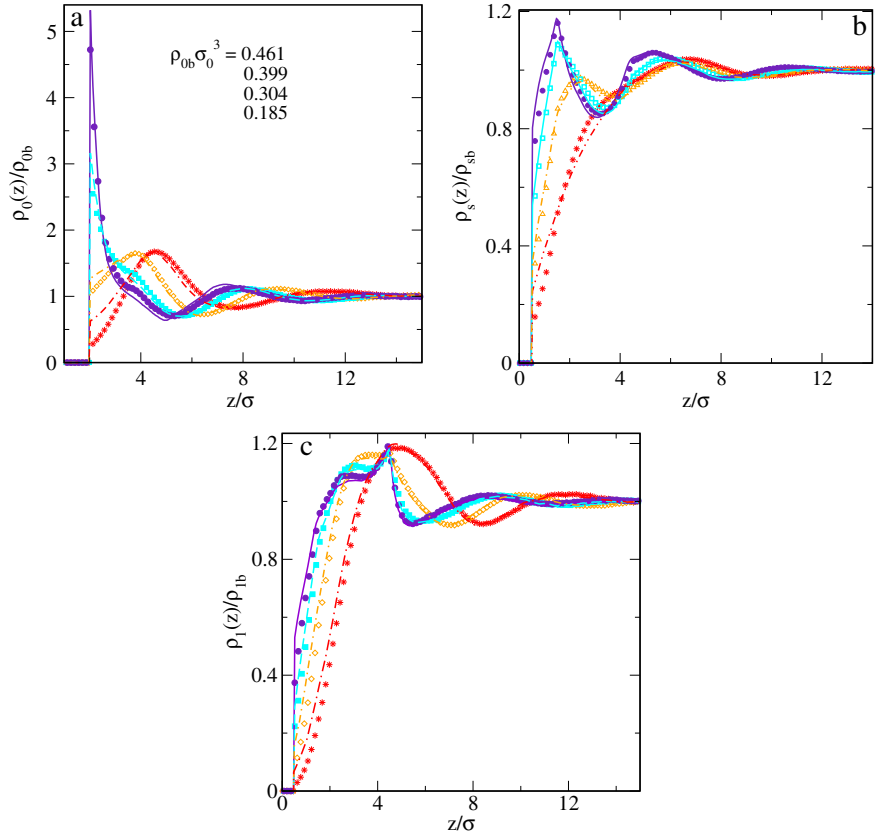

Fig. 8. Density profiles of cores (part a), all segments (part b) and of tethered segments (part c) reduced by corresponding bulk densities. Computer simulation data are marked as symbols and density functional results – by lines. The consecutive pairs of curves from top correspond to the bulk densities ρ_{0b} given in part a. The color codes are identical as in Fig. 2a. All calculations are for the model M.

its position is the same as for bare core particles. This is the consequence of sliding all ligands away from the surface. The behavior of the model M resembles the behavior of loosely coupled mixture of large core particles and ligands.

We have evaluated the mass dipoles that characterize the distribution of segments around the cores. The length of the mass dipoles for the model M is almost two times larger than for the model F and also the orientational effects of the mass dipoles are much more pronounced for the model M.

In order to describe the density profiles for the model M we have used a version of the density functional approach. This theory works reasonable well at higher densities and the more significant deviations are observed for low values of ρ_{0b}, where the hard-sphere contribution to the system free energy becomes less significant. We have also discussed the origin of the presence of cusps on the segment density profiles.

In our opinion it would be of interest to extend the present study to the case of hairy molecules confined between two hard walls (in slit-like pores). The presence of two walls should lead to more pronounced differences between two investigated models. Also, in is interesting to check how the changes of the length and number of ligands, under constraint of constancy of the total number of segments $L \times N$ would influence of the structure of adsorbed layers. All these problems are under study in our laboratory.

Acknowledgments

M.B. and S.S. acknowledge support from NCN Poland under Grant No. 2015/17/B/ST4/03615.

References

[1] O. Bernard, L. Blum, Thermodynamics of a model for flexible polyelectrolytes in the binding mean spherical approximation, J. Chem. Phys. 112 (2000) 7227.
[2] J.W. Jiang, L. Blum, O. Bernard, J.M. Prausnitz, Thermodynamic properties and phase equilibria of charged hard sphere chain model for polyelectrolyte solutions, Molec. Phys. 99 (2001) 1121.
[3] I.A. Protsykevytch, Y.V. Kalyuzhnyi, M.F. Holovko, L. Blum, Solution of the polymer mean spherical approximation for the totally flexible sticky two-point electrolyte model, J. Molec. Liq. 1 (1997) 73–74.
[4] D. Bratko, H.L. Friedman, S.H. Chen, L. Blum, Interpretation of the intermicellar structure factors in the hypernetted-chain Percus-Yevick approximation, Phys. Rev. A 34 (1986) 2215.
[5] O. Pizio, L. Blum, Analytic solution of the mean spherical approximation for a dipolar hard-sphere fluid with intracore anisotropic sticky interactions, Phys. Rev. E 52 (1995) 572.
[6] A. Maestro, E. Guzmán, F. Ortega, R.G. Rubio, Contact angle of micro-and nanoparticles at fluid interfaces, Curr. Opin. Colloid Interface Sci. 19 (2014) 355.
[7] J. Reguera, E. Ponomarev, T. Geue, F. Stellacci, F. Bresme, M. Moglianetti, Contact angle and adsorption energies of nanoparticles at the air-liquid interface determined by neutron reflectivity and molecular dynamics, Nanoscale 7 (2015) 5665.
[8] S. Crossley, J. Faria, M. Shen, D.E. Resasco, Solid nanoparticles that catalyze biofuel upgrade reactions at the water/oil interface, Science 327 (2010) 68.
[9] A. Verma, F. Stellacci, Effect of surface properties on nanoparticle-cell interactions, Small 6 (2010) 12.
[10] A. Böker, J. He, T. Emrick, T.P. Russell, Self-assembly of nanoparticles at interfaces, Soft Matter 3 (2007) 1231.
[11] J. Wang, P. Kanjanaboos, S.P. McBride, E. Barry, X.M. Lin, H.M. Jaeger, Mechanical properties of self-assembled nanoparticle membranes: stretching and bending, Faraday Discuss. 181 (2015) 325.
[12] J. He, X.M. Lin, H. Chan, L. Vukovi, P. Kral, H.M. Jaeger, Diffusion and filtration properties of self-assembled gold nanocrystal membranes, Nano Lett. 11 (2011) 2430.
[13] X. Tian, H. Zheng, U. Mirsaidov, Aggregation dynamics of nanoparticles at solid-liquid interfaces, Nanoscale 9 (2017) 10044.
[14] E. Miele, S. Raj, Z. Baraissov, P. Král, U. Mirsaidov, Dynamics of templated assembly of nanoparticle filaments within nanochannels, Adv. Mater. 295 (2017)1702682.
[15] S.W. Chee, Z. Baraissov, N.D. Loh, P.T. Matsudaira, U. Mirsaidov, Desorption–mediated motion of nanoparticles at the liquid-solid interface, J. Phys. Chem. C 120 (2016)20462.
[16] S. A. Vasudevan, A. Rauh, L. Barbera, M. Karg, L. Isa, Stable in bulk and aggregating at the interface: comparing core-shell nanoparticles in suspension and at fluid interfaces. Langmuir, Just Accepted Manuscript DOI: 10.1021/acs.langmuir.7b02015.
[17] P. Hanarp, D.S. Sutherland, J. Gold, B. Kasemo, Influence of polydispersity on adsorption of nanoparticles, J. Coll. Interface Sci. 241 (2001) 26.
[18] J. Lu, D. Liu, X. Yang, Y. Zhao, H. Liu, H. Tang, F. Cui, Molecular dynamics simulations of interfacial interactions between small nanoparticles during diffusion-limited aggregation, Appl. Surf. Sci. 357 (2015) 1114.
[19] J. Che, A. Jawaid, C.A. Grabowski, Y.J. Yi, G.C. Louis, S. Ramakrishnan, R.A. Vaia, Stability of polymer grafted nanoparticle monolayers: impact of architecture and polymer-substrate interactions on dewetting, ACS Macro Lett. 5 (2016) 1369.
[20] K. Binder, A. Milchev, Polymer brushes on flat and curved surfaces: how computer simulations can help to test theories and to interpret experiments, J. Polym. Sci. B. Polym. Phys. 50 (2012) 1515.
[21] A. Chremos, A.Z. Panagiotopoulos, H.Y. Yu, D.L. Koch, Structure of solvent-free grafted nanoparticles: molecular dynamics and density-functional theory, J. Chem. Phys. 135 (2011) 11901.
[22] K.M. Sulerno, A.E. Ismail, J.M. Lane, S.G. Grest, Coating thickness and coverage effects on the forces between silica nanoparticles in water., J. Chem. Phys. 140 (2014)194904.
[23] B. Hong, A. Chremos, A.Z. Panagiotopoulos, Dynamics in coarse-grained models for oligomer-grafted silica nanoparticles, J. Chem. Phys. 136 (2012)204904.
[24] R. Evans, The nature of the liquid-vapour interface and other topics in the statistical mechanics of non-uniform, classical fluids, Adv. Phys. 28 (1979) 143.
[25] J. Wu, Density functional theory for chemical engineering: from capillarity to soft materials, AIChE J. 52 (2006) 1169.
[26] J. Wu (Ed.), Variational Methods in Molecular Modeling, Springer Science+Business Media Singapore.2017,
[27] A. Patrykiejew, O. Pizio, S. Sokołowski, Statistical Surface Thermodynamics, In Surface and Interface Science: Solid-Gas Interfaces II, in: K. Wandelt (Ed.), vol. 6, Wiley-VCH Verlag GmbH and Co. KGaA, Weinheim, Germany, 2016, pp. 883–1253.
[28] J. Hughes, E.J. Krebs, D. Roundy, A classical density-functional theory for describing water interfaces, J. Chem. Phys. 138 (2013)024509.
[29] A. Haghmoradi, L. Wang, W.G. Chapman, A density functional theory for colloids with two multiple bonding associating sites, J. Phys.: Condens. Matter 28 (2016)244009.
[30] O. Pizio, S. Sokołowski, Advances in the theoretical description of solid-electrolyte solution interfaces in solid state electrochemistry II, in: V.V. Kharton (Ed.), Wiley-VCH, Weinheim, 2011, pp. 73–124. Chapter 3.
[31] G.M. Range, S.H.L. Klapp, Density functional study of the phase behavior of asymmetric binary dipolar mixtures, Phys. Rev. E 69 (2004)041201.
[32] A.M. Somoza, E. Chacón, L. Mederos, P. Tarazona, A model for membranes, vesicles and micelles in amphiphilic systems, J. Phys.: Condens Matter 7 (1995) 5753.
[33] M. Borówko, T. Pöschel, S. Sokoowski, T. Staszewski, Janus particles at walls modified with tethered chains, J. Phys. Chem B 117 (2013) 1166.
[34] D. Chandler, J.D. McCoy, S.J. Singer, Density functional theory of nonuniform polyatomic systems. i. General formulation, J. Chem. Phys. 85 (1986) 5971.
[35] J. Wu, Z. Li, Density-functional theory for complex fluids, Annu. Rev. Phys. Chem. 58 (2007) 85.
[36] L.J.D. Frink, A.G. Salinger, Two- and three-dimensional nonlocal density functional theory for inhomogeneous fluids II. Solvated polymers as a benchmark problem, J. Comput. Phys. 159 (2000) 425.
[37] M.P. Sears, L.J.D. Frink, A new efficient method for density functional theory calculations of inhomogeneous fluids, J. Comput. Phys. 190 (2003) 184.
[38] A. Nold, B.D. Goddard, P. Yatsyshin, N. Savva, S. Kalliadasis, Pseudospectral methods for density functional theory in bounded and unbounded domains, J. Comput. Phys. 334 (2017) 639.
[39] J. Jiang, D. Cao, Modeling of highly efficient drug delivery system induced by self-assembly of nanocarriers. A density functional study, Sci. China: Chem. 56 (2012) 249.
[40] E. Sauer, J. Gross, Classical density functional theory for liquid-fluid interfaces and confined systems: a functional for the perturbed-chain polar statistical associating fluid theory equation of state, Ind. Eng. Chem. Res. 56 (2017) 4119.
[41] C. Chen, P. Tang, F. Qiu, A.C. Shi, Density functional study for homodendrimers and amphiphilic dendrimers, J. Phys. Chem. B 120 (2016) 5553.
[42] P. Cremer, M. Heinen, A.M. Menzel, H. Löwen, A density functional approach to ferrogels, J. Phys.: Condens. Matter 29 (2017)275102.
[43] M. Marechal, S. Dussi, M. Dijkstra, Density functional theory and simulations of colloidal triangular prisms, J. Chem Phys. 146 (2017)124905.
[44] F.J. Blas, L.F. Vega, Thermodynamic properties and phase equilibria of branched chain fluids using first- and second-order Wertheim's thermodynamic perturbation theory, J. Chem. Phys. 115 (2001) 3906.
[45] A. Malijevský, P. Bryk, S. Sokołowski, Density functional approach for inhomogeneous star polymer fluids, Phys. Rev E 72 (2005)032801.
[46] D. Cao, T. Jiang, J. Wu, A hybrid method for predicting the microstructure of polymers with complex architecture: combination of single-chain simulation with density functional theory, J. Chem. Phys. 124 (2006)164904.
[47] E.S. McGarrity, J.M. Thijssen, N.A.M. Besseling, Fluids density functional theory studies of supramolecular polymers at a hard surface, J. Chem. Phys. 133 (2010)084902.
[48] B.D. Marshall, W.G. Chapman, Higher order classical density functional theory for branched chains and rings, J. Phys. Chem. B 115 (2011) 15036.
[49] J. Jiang, X. Xu, D. Cao, Density functional theory for inhomogeneous ring polymeric fluids, Phys. Rev. E 86 (2012)041805.
[50] J. Jiang, X. Xu, J. Huang, D. Cao, Density functional theory for rod-coil polymers with different size segments, J. Chem. Phys. 135 (2011)054903.
[51] R. Roth, R. Evans, A. Lang, G. Kahl, Fundamental measure theory for hard–sphere mixtures revisited: the White Bear version, J. Phys.: Condens. Matter 14 (2002) 12063.
[52] D.P. Cao, J.Z. Wu, Density functional theory for semiflexible and cyclic polyatomic fluids, J. Chem. Phys. 121 (2004) 4210.
[53] M.S. Wertheim, Thermodynamic perturbation theory of polymerization, J. Chem. Phys. 87 (1987) 7323.
[54] E. Bianchi, B. Capone, G. Kahl, C.N. Likos, Soft-patchy nanoparticles: modeling and self-organization, Faraday Discuss. 181 (2015) 123.
[55] I.C. Gârlea, E. Bianchi, B. Capone, L. Rovigatti, C.N. Likos, Hierarchical self-organization of soft patchy nanoparticles into morphologically diverse aggregates, Curr. Opin. Colloid Interface Sci. 30 (2017) 1.
[56] K.H. Ku, Y.J. Kim, G.R. Yi, Y.S. Jung, B.J. Kim, Soft patchy particles of block copolymers from interface-engineered emulsions, ACSNano 9 (2015) 11333.
[57] M.S. Nikolic, C. Olsson, A. Salcher, A. Kornowski, A. Rank, R. Schubert, A. Froemsdorf, H. Weller, S. Foerster, Micelle and vesicle formation of amphiphilic nanoparticles, Angew. Chem. Int. Ed 48 (2009) 2752.
[58] J.M. Ilnytskyi, A. Slyusarchuk, M. Saphiannikova, Photocontrollable self--assembly of azobenzene-decorated nanoparticles in bulk: computer simulation study, Macromolecules 49 (2016) 9272.
[59] J.M. Ilnytskyi, A. Slyusarchuk, M. Saphiannikova, Photo-controllable percolation of decorated nanoparticles in a nanopore: molecular dynamics simulation study, Math. Model. Comput. 3 (2016) 33.
[60] S.A.J. van der Meulen, G. Helms, M. Dogterom, Solid colloids with surface-mobile linkers, J. Phys.: Condens. Matter 27 (2015)233101.
[61] F. Lo Verso, S.A. Egorov, A. Milchev, K. Binder, Spherical polymer brushes under good solvent conditions: molecular dynamics results compared to density functional theory, J. Chem. Phys. 133 (2010)184901.
[62] F. LoVerso, S.A. Egorov, K. Binder, Interaction between polymer brush-coated spherical nanoparticles: effect of solvent quality, Macromolecules 45 (2012) 8892–8902.

[63] Ł. Baran, S. Sokołowski, Effective interactions between a pair of particles modified with tethered chains, J. Chem. Phys. 044903 (2017) 147.
[64] H. Chen, E. Ruckenstein, Micellar structures in nanoparticle- multiblock copolymer complexes, Langmuir 30 (2014) 3723.
[65] S.B. Jabes, H.O.S. Yadav, S.K. Kumar, C. Chakravarty, Fluctuation- driven anisotropy in effective pair interactions between nanoparticles: thiolated gold nanoparticles in ethane, J. Chem. Phys. 141 (2014)154904.
[66] Ł. Baran, S. Sokołowski, A comparison of molecular dynamics results for two models of nanoparticles with fixed and mobile ligands in two-dimensions, Appl. Surf. Sci. 396 (2017) 1343.
[67] S. Plimpton, Fast parallel algorithms for short-range molecular- dynamics, J. Comput. Phys. 117 (1995) 1.
[68] For the description of the package see http://lammps.sandia.gov.
[69] Y. Tang, On the first-order mean spherical approximation, J. Chem. Phys. 118 (2003) 4140.
[70] J.S. Rowlinson, Virial expansions in an inhomogeneous system, Proc. R. Soc. Lond. A Math. Phys. Sci. 402 (1985) 67.
[71] S. Sokołowski, J. Fischer, Relation between born-green-yvon solutions and chemical potential for a fluid inside a pore, J. Chem. Phys. 93 (1990) 6787.
[72] M. Borówko, W. Rżysko, S. Sokołowski, T. Staszewski, Density functional approach to adsorption and retention of spherical molecules on surfaces modified with end-grafted polymers, J. Phys. Chem. B 113 (2009) 4763.